A New Method to Evaluate and Modify Chang'E-2 Microwave Radiometer Low-Frequency Data Constrained From Diviner Thermal Measurements

Guangfei Wei, Shane Byrne, Xiongyao Li, Jianqing Feng, and Matthew A. Siegler

***Abstract*— Microwave emission is influenced by regolith thermophysical properties that can reveal the geological evolution of the Moon. Lunar near-surface microwave emission has been systematically investigated by the microwave radiometer (MRM) onboard Chinese Chang'E-2 (CE-2) lunar satellite. However, recent work showed that global calibration issues were causing discrepancies between CE-2 observations and theoretical simulations at 3.0- and 7.8-GHz channels, which influences data interpretations and applications. In this study, we use a new method to improve thermal models by employing the bolometric brightness temperature and thermophysical property of subsurface structure derived from high quality and repeated coverage Diviner data. The derived subsurface temperatures make it possible for us to improve the accuracy of microwave brightness temperature (T_B) simulation within 70°N/S latitudes. We evaluate the MRM data quantitatively by comparing the global T_B between modeled values and CE-2 observations (i.e., offset values) at different local times (LTs) and latitudes. The results show that offset values of the two channels vary significantly with LT, especially near 06:00 and 18:00. However, the 7.8-GHz channel presents greater (∼12k in average) calibration uncertainties than the 3.0-GHz channel. In addition, the offset of both the two channels becomes complex at high latitudes but presents an obvious north–south asymmetry. Finally, we modify the MRM data according to different offsets at different LTs and latitudes. The modified global T_B maps provide us a new view to characterize the lunar near-surface thermal environment, especially for low-T_B spots that are related to the elevated rock abundance and crater degradation.**

***Index Terms*— Brightness temperature, Chang'E, Diviner, modification, Moon, thermal model.**

I. Introduction

LUNAR surface and subsurface temperatures are of great interest for investigating the thermal properties of regolith, interior heat flow, and the thermal stability of buried water ice at cold traps located in polar regions [1]–[3]. Surface/subsurface brightness temperatures have been obtained by ground-based observations from infrared to radio frequency [4], [5]. However, these early measurements had large calibration uncertainties, and only the nearside of the Moon could be observed. The Apollo 15 and 17 *in situ* heat flow experiments provided constraints on the subsurface thermal regime and thermophysical properties at those sites but did not measure the subsurface thermal environment on a global scale.

Compared with visible and infrared radiation, microwaves can penetrate to (or escape from) a greater depth, which depends on subsurface permittivity. In 2007 and 2010, China successfully launched the Chang'E-1 (CE-1) and Chang'E-2 (CE-2) lunar satellites; both missions ended after ∼1.5 and ∼1 year operations, respectively [6], [7]. The microwave radiometers (MRMs), including four channels onboard CE-1 and CE-2, were first designed to measure lunar subsurface microwave emission to investigate regolith thickness and estimate the content of Helium-3 resources [8]. The altitude of CE-2 is half that of CE-1 (∼200 km), so its spatial resolution is approximately double. Furthermore, the CE-2 observations covered the lunar surface at all local times (LTs), whereas CE-1's observations are only at noon and midnight [6]. Therefore, the CE-2 MRM data can reveal the diurnal variation of subsurface temperatures in more detail.

Despite these advantages, recent work [9]–[11] proposed that there are obviously calibration uncertainties for CE-2 low-frequency channels (i.e., 3.0 and 7.8 GHz) when comparing to numerical simulations. It has been reported that the calibration issue might be caused by: 1) lunar surface heat contaminations [9], [12] and 2) the reorientation of MRM's cold horns toward the Sun when the satellite crossing terminators [10]. This might lead to great ambiguity for interpreting lunar regolith property and subsurface thermal regime. Hu *et al.* [9] investigated the first factor (latitude effect) by comparing CE-1/2 MRM data with theoretical simulations. However, they only study the Apollo 15 and 17 landing areas without considering the LT and latitude effects. Feng *et al.* [10] considered the second factor (LT effect) by comparing the CE-2 MRM data and simulations only at the highland of equator. The effect of LT and latitude on CE-2 MRM data calibration issue on a global scale has not been investigated systematically. To better understand lunar near-surface thermal behavior globally, the calibration

Manuscript received September 24, 2020; revised January 26, 2021 and March 31, 2021; accepted April 22, 2021. The work of Guangfei Wei was supported in part by the B-Type Strategic Priority Program of the Chinese Academy of Sciences under Grant XDB 41000000 and in part by the National Natural Science Foundation of China under Grant 41803052 and Grant 41931077. *(Corresponding author: Xiongyao Li.)*

Guangfei Wei and Xiongyao Li are with the Center for Lunar and Planetary Sciences, Institute of Geochemistry, Chinese Academy of Sciences (CAS), Guiyang 550081, China, and also with the CAS Center for Excellence in Comparative Planetology, Hefei 232006, China (e-mail: weiguangfei@mail.gyig.ac.cn; lixiongyao@vip.skleg.cn).

Shane Byrne is with the Lunar and Planetary Laboratory, The University of Arizona, Tucson, AZ 85721 USA.

Jianqing Feng and Matthew A. Siegler are with the Planetary Science Institute, Tucson, AZ 85719 USA.

Digital Object Identifier 10.1109/TGRS.2021.3077890

uncertainty of CE-2 MRM diurnal observations needs to be evaluated and modified accurately before further interpretation and application. Here, we only evaluate the CE-2 MRM low-frequency data that are limited within 70°N/S latitudes to avoid additional uncertainties caused by surface slopes and shadows at high latitudes [13].

The Lunar Reconnaissance Orbiter (LRO) was launched in 2009 and is still in operation. Its Diviner instrument systematically maps the lunar surface temperature globally [14]. The repeated coverage of thermal infrared data has been used to derive the surface bolometric brightness temperature ($T_{\rm bol}$) at all lunar locations and LTs [2], [15]. Recently, a global $T_{\rm bol}$ data product with a spatial resolution of $0.5^\circ \times 0.5^\circ$ has been derived using large numbers of Diviner observations [15]. Here, we use this product as a surface thermal constraint to derive subsurface temperature profiles.

In addition, in order to calculate subsurface temperature profiles accurately, knowledge of the thermophysical properties of the regolith at any location on the Moon is required. Terrestrial measurements of returned Apollo samples can provide detailed thermophysical parameters; however, this may only reflect the properties at specific sites. Based on regolith temperatures derived from Diviner data [16], Hayne *et al.* [3] recently derived the global thermal inertial of the surface at 273 K and how thermophysical properties vary with depth (via the H parameter, discussed later). Following Hayne *et al.* [3], we use the H parameter to calculate the subsurface density and thermal conductivity that are also used to constrain a thermal model.

To convert subsurface temperatures into microwave emission, it is necessary to get the dielectric properties of the regolith, which depends on composition and radio frequency [10], [11]. Here, we use estimates of the titanium abundances to deduce the dielectric constant profile on the Moon.

As noted above, microwave measurements are complementary to thermal infrared observations, which can "see" greater depths of lunar regolith, especially at low frequency (long wavelength) of the MRM. However, the MRM data with calibration issues would cause a great ambiguity of geological interpretation. The modified MRM's low-frequency data of this work can reveal accurate and detailed information of subsurface, for example, subsurface temperature, internal heat flow, dielectric permittivity of near-surface material, regolith thickness, and rock abundance (RA). This will help us to better understand the geologic evolution of the Moon.

In this study, we first improve the thermal model from constraints of Diviner measurements and H parameter. We calculate the diurnal variation of subsurface temperatures and model microwave brightness temperatures (T_B) at low frequency of MRM. We then evaluate MRM's observations by comparing with modeled T_Bs at different latitude bands and LT ranges. Third, we modify the MRM data on a global scale (within 70° N/S) considering the effects of latitude and LT. Finally, we discuss three factors (seasonal effects, RA, and titanium content) that can influence the T_B simulation and the potential application of modified T_B.

II. Datasets

A. CE-2 MRM Data

The MRM onboard CE-2 globally mapped microwave emission of the Moon in a polar orbit ∼15 times with four channels, i.e., 3.0, 7.8, 19.35, and 37 GHz in a nadir viewing mode at an altitude of 100 km [7]. The MRM measured brightness temperature with 0.5 K accuracy and a spatial resolution of 25 km for the first channel and 17.5 km for all others. During observations, a two-point calibration method was used as the same as CE-1 to derive the brightness temperature, T_B, with alternating views of surface and cold space [8]. CE-2 observations from October 15, 2010, to May 20, 2011, were archived in the Planetary Data System (PDS), and the Level 2C data are publicly available.

Several researchers proposed that there are large discrepancies between CE-2 MRM low-frequency observations and T_B simulations [9]–[11]. This indicates that there might be calibration uncertainties caused by heat contamination, especially at the LTs 06:00/18:00 when the calibration horn antenna reoriented and pointed toward the Sun [10]. The relatively large 3.0- and 7.8-GHz cold horns are heated by solar illumination, which results in greater calibration uncertainties [10].

B. Diviner Bolometric Brightness Temperature Data

Diviner is a nine-channel filter radiometer that has systematically mapped the lunar surface temperature since 2009. Channels 1 and 2, with wavelength range 0.35–2.8 μm, are designed to measure lunar surface reflected solar radiation. The remaining channels (3–9) measure the emitted infrared radiation with passbands of 2.8–400 μm. Each channel observes the Moon with an array of 21 detectors in a push-broom configuration [14]. After transitioning into a circular orbit at an average altitude ∼50 km [15], Diviner observes the lunar surface with a spatial resolution of ∼200 m and a ground track swath of 3.4 km.

Due to its lack of atmosphere, slow rotation, and highly insulating surface dust (∼2 cm thick), the lunar surface temperature can reach equilibration with solar radiation in the daytime. At night, the surface/subsurface temperature decreases gradually due to heat loss until dawn. The bolometric brightness temperature, $T_{\rm bol}$, is the measure of spectral integration of surface infrared radiation and is determined from the brightness temperatures of the seven Diviner infrared channels [2]. Diviner-based $T_{\rm bol}$ has been binned at $0.5^\circ \times 0.5^\circ$ and 0.25-h LT from July 5, 2009, to April 1, 2015 and has been archived at the PDS Geosciences Node. Here, we use the $T_{\rm bol}$ data that include information on the surface emissivity, albedo, effective solar irradiation, surface slope, and light scattered from surrounding terrain as a surface thermal constraint [17].

C. H Parameter

In order to derive the global distribution of time- and depth-dependent temperatures, it is important to constrain the thermal properties of the subsurface, which conducts heat downward from the surface. Vasavada *et al.* [18] introduced the H parameter to constrain the bulk density of the regolith near

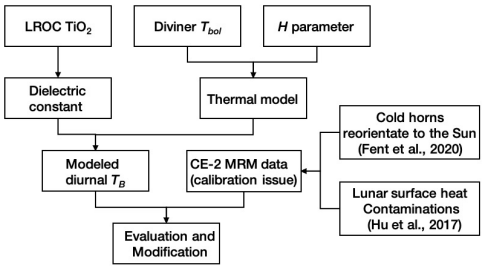

Fig. 1. Work flow of brightness temperature simulation, evaluation, and modification.

the Moon's equator based on the repeated coverage Diviner data. Hayne *et al.* [3] then derived the global H parameter within 70°N/S latitudes at 128 pixels per degree (ppd) from nighttime regolith temperatures [16].

We use the H parameter derived by Hayne *et al.* [3] to calculate the profiles of density and thermal conductivity. In this study, we reduced this 128 ppd dataset to $0.5^\circ \times 0.5^\circ$ by averaging the data points within each cell. Larger values of the H parameter indicate highly insulating material, whereas smaller values denote a denser and more conductive regolith. Based on the global H parameter dataset as well as constrained by $T_{\rm bol}$, we can calculate subsurface temperature profiles globally.

D. Global Distribution of Titanium

Recent studies about analyzing CE-2 MRM data suggest that microwave emission is strongly dependent on titanium content and frequency [10], [11]. As the surface reflectance of the Moon is dominated by variation of chemical composition [19], spectral data can be interpreted in terms of mineral concentrations. The Clementine Ultraviolet/Visible spectral data were first used to derive the global distribution of TiO_2 at 100 m/pixel by Lucey *et al.* [20], and their algorithms were revised later by Gillis *et al.* [21] based on dual-regression methods. Recently, more accurate TiO_2 abundance was derived from LRO wide-angle camera (WAC) observations with a spatial resolution of 400 m/pixel [19]. Note that since the detection limit of WAC TiO_2 content at lunar mare is 2 wt%, we set the nonmare areas TiO_2 content as zero following Siegler *et al.* [11] to apply their dielectric models of lunar maria and highlands.

III. Methodology

In order to model and evaluate CE-2 MRM data, it is important to derive subsurface temperatures and model brightness temperature accurately. Here, we improve the 1-D thermal model by employing the global H parameter based on our previous Diviner $T_{\rm bol}$ data constrained thermal model (see Fig. 1) [17], that is, the H parameter used here to constrain subsurface thermophysical properties in terms of density and thermal conductivity at each bin. Note that the effect of rock concentration on near-surface thermal behavior is not considered in our thermal model.

In addition, we model the diurnal variation of T_B at 3.0 and 7.8 GHz of each bin after running the above thermal and dielectric constant models. Finally, we compare the global MRM observations and T_B simulations at different LTs ranges to evaluate and modify CE-2 MRM observations.

A. Improved 1-D Thermal Model

Variations of subsurface temperature are controlled by surface insolation, conduction, interior heat flow, and outward reradiation. The regolith can be considered as a semi-infinite solid material, and the time- and depth-dependent temperature, $T(t, z)$, can be calculated by the 1-D heat diffusion equation

$$\rho(z)c_p(T)\frac{\partial T(t,z)}{\partial t} = \frac{\partial}{\partial z}\left[K(T(t,z))\frac{\partial T(t,z)}{\partial z}\right] \quad (1)$$

where $\rho(z)$ is the bulk density, $c_p(T)$ is the specific heat, $c_p = c_0 + c_1 T + c_2 T^2 + c_3 T^3 + c_4 T^4$ [3], and K is the thermal conductivity. A model showing that density increases with depth was accurately derived based on the fitting equatorial Diviner data [18]. The density profile was modified later by Hayne *et al.* [3] for global application as follows:

$$\rho(z) = \rho_d - (\rho_d - \rho_s)e^{-\frac{z}{H}} \quad (2)$$

where ρ_s and ρ_d are densities at surface and depth $z \gg H$, respectively. The thermal conductivity is also controlled by composition and density over the range of subsurface temperatures [22] in the equation

$$K = K_c\left[1 + \chi\left(\frac{T(t,z)}{350}\right)^3\right] \quad (3)$$

where K_c is the contact conductivity that is assumed to be linearly proportional to density [3] and χ is a dimensionless radiative conductivity parameter. Also, K_c is expressed as

$$K_c = K_d - (K_d - K_s)\frac{\rho_d - \rho(z)}{\rho_d - \rho_s} \quad (4)$$

where the constants K_s and K_d are the contact conductivity at the surface and the depth, $z \gg H$, respectively. Thus, the H parameter governs how subsurface density and thermal conductivity increase with depth. Specific heat capacity only depends on temperature (see [3] for a more detailed discussion).

Mathematically, two boundary conditions are needed to solve (1). The lower boundary at the depth of z_d has a constant upward heat flow (Q), which can be determined by

$$K\frac{\partial T}{\partial z}\bigg|_{z=z_d} = -Q. \quad (5)$$

Here, the global mean heat flow value that is derived from surface thorium abundance and inferred crustal thickness was used in our thermal model [23]. Also, the bottom depth z_d is given as 5 m, which is greater than the 3-GHz channel's sensed depth [10].

At the surface, the upper boundary condition is the absorbed insolation and conduction that are balanced against thermal emissions. Global simulation is complex since multiple factors, e.g., albedo, emissivity, and surface roughness, controlled lunar surface thermal environment. Instead, we use the diurnal variation temperatures $T_{\rm bol}$ that include all these factors as the upper boundary condition (more details can be seen in our previous work [17]).

TABLE I
PARAMETERS USED IN THE THERMAL MODEL AND LOSS TANGENT MODEL

Parameter	Symbol	Value	Reference
Surface layer density	ρ_s	1100 kg m^{-3}	[3]
Deep layer density	ρ_d	1800 kg m^{-3}	[3]
Surface layer conductivity	K_s	7.4×10^{-4} W m^{-1} K^{-1}	[3]
Deep layer conductivity	K_d	3.4×10^{-3} W m^{-1} K^{-1}	[3]
Coefficients of specific heat function	c_0	-3.6125J kg^{-1} K^{-1}	[3]
	c_1	2.7431 J kg^{-1} K^{-2}	[3]
	c_2	2.3616×10^{-3} J kg^{-1} K^{-3}	[3]
	c_3	-1.2340×10^{-5} J kg^{-1} K^{-4}	[3]
	c_4	8.9093×10^{-9} J kg^{-1} K^{-5}	[3]
Radiative conductivity parameter	χ	2.7	[18]
Interior heat flux	Q	0.012 W m^{-2}	[23]
Mare fits constants	a	-2.65	[11]
	b	-0.0025	[11]
	c	-0.958	[11]
Highlands fits constants	a	-3.79	[11]
	b	0.069	[11]
Light speed	c	3×10^8 m s^{-1}	-
Relative permeability in free space	μ	1.0	-

B. Subsurface Microwave Emission Model

Terrestrial experiments on Apollo samples between 10 and 30 GHz showed that ilmenite plays an important role in electromagnetic absorption [24]. The relative dielectric constant, ε_r, determines the behavior of electromagnetic waves in a medium and includes a real part, ε', and an imaginary part, ε'', i.e., $\varepsilon_r = \varepsilon' + i\varepsilon''$. Measurements have shown that ε' is insensitive to frequency but is dependent on bulk density [24] and can be written as

$$\varepsilon' = 1.919^{\rho(z)} \tag{6}$$

where ε'' influences the stored electromagnetic energy and is a function of frequency, bulk density, and chemical composition [24].

Montopoli *et al.* [25] proposed a relationship between frequency (f) and loss tangent ($\tan\delta = \varepsilon''/\varepsilon'$). Also, Siegler *et al.* [11] employed a similar form and improved the parameters by fitting the CE-2 MRM data. Following their work, the loss tangent of lunar mare and highland can be expressed as:

$$\tan\delta_{\text{mare}} = 10^{[0.312\rho+a+S(f^b+c)]} \tag{7}$$

$$\tan\delta_{\text{highlands}} = 10^{[0.312\rho+a+f^b]} \tag{8}$$

where S is the content of TiO_2 in wt% and a, b and c are coefficients. It is worth noting that $\tan\delta_{\text{highlands}}$ is independent of S because the TiO_2 content in nonmare areas is set as zero.

For the nadir viewing geometry of CE-2 MRM (where perpendicular and parallel polarizations are equal) [26], [27], the microwave brightness temperature can be written as

$$T_B(f,t) = (1-r)\int_0^\infty \kappa_\alpha(z)\ T(z,t)e^{-\int_0^z \kappa_\alpha(z')dz'}dz \tag{9}$$

where $r = \left|(1-\sqrt{\varepsilon'}/1+\sqrt{\varepsilon'})\right|^2$ is the smooth surface reflectivity, $\kappa_\alpha = (4\pi f/c)\text{Im}(\sqrt{\mu\varepsilon_r})$ is the absorption coefficient, c is light speed in the vacuum, and μ is the relative permeability in free space. Based on the above equations and the datasets of T_{bol}, H parameter, and TiO_2, we can model T_B globally for each microwave frequency. The model parameters and corresponding references are listed in Table I.

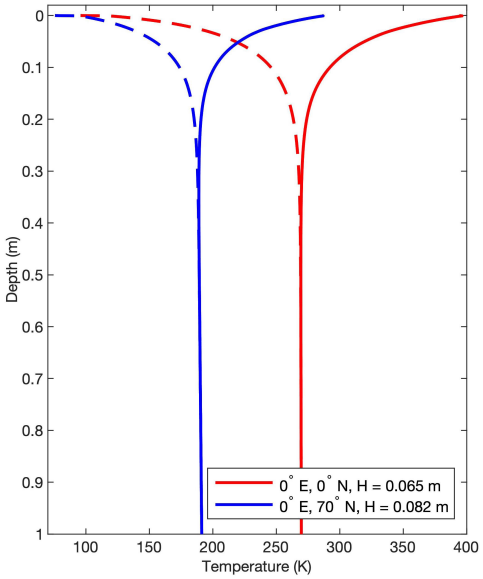

Fig. 2. Comparison of temperature profiles at the cell of 0° E, 0° N (red curves) and 0° E, 70° N (blue curves). The solid curves are the maximum temperature profiles, and the dashed curves are the minimum temperature profiles. The H parameters corresponding to each cell are derived from the Diviner data based on the work in [3].

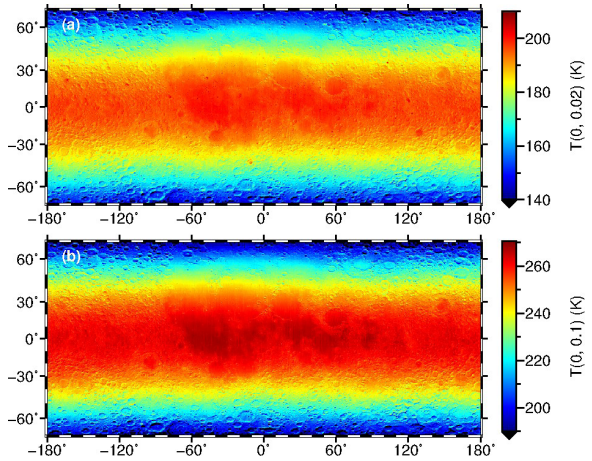

Fig. 3. Calculated subsurface temperatures at the depths of (a) 0.02 m, $T(0, 0.02)$, and (b) 0.1 m, $T(0, 0.1)$, at midnight.

IV. RESULTS

In this section, we first present the calculated subsurface temperatures to show the effectiveness of our improved thermal model. The diurnal variation of subsurface temperatures enables us to model microwave emission in both the 3.0- and 7.8-GHz channels in a lunar day. Subsequently, a quantitative evaluation and modification of global CE-2 MRM data was presented.

A. Subsurface Temperature

Many methods have investigated lunar regolith thickness, such as Apollo *in situ* measurements [24], crater morphology and size-frequency distribution [28], and radar and microwave

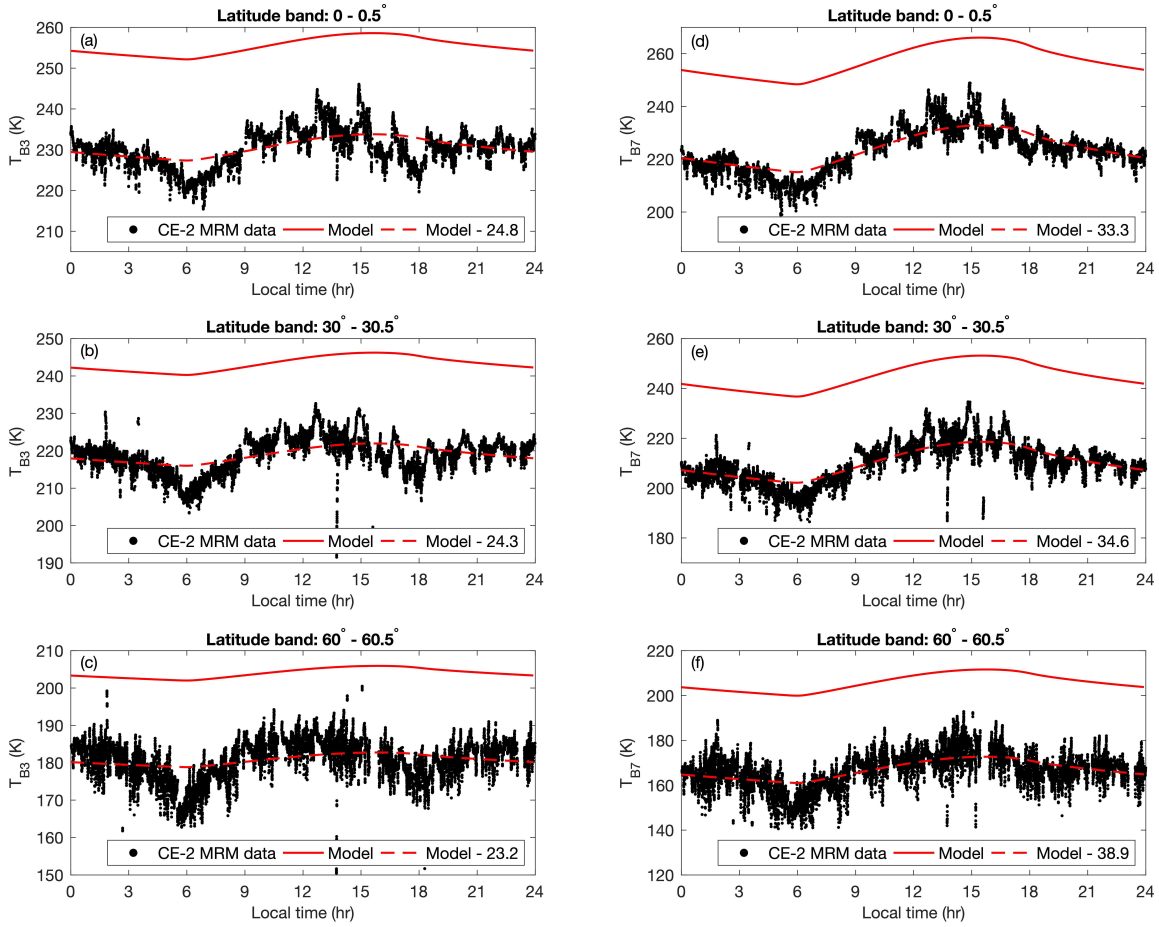

Fig. 4. Comparison between diurnal variations of CE-2 MRM data and T_B simulations at 3.0 GHz (left column) and 7.8 GHz (right column). (a) and (d), (b)–(e), and (c) and (f) Latitude bands of 0–0.5° N, 30–30.5° N, and 60–60.5° N, respectively.

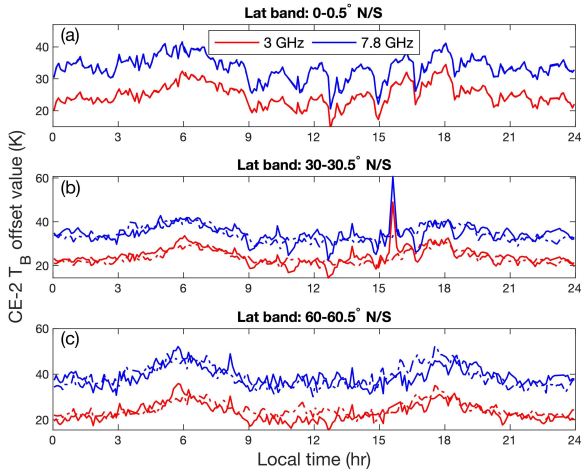

Fig. 5. T_B offsets vary as a function of LT at latitude bands of (a) 0–0.5° N/S, (b) 30–30.5° N/S, and (c) 60–60.5° N/S. The solid and dashed-dotted lines indicate northern and southern latitudes, respectively. The offset is averaged from each latitude band with an LT interval 0.1 h.

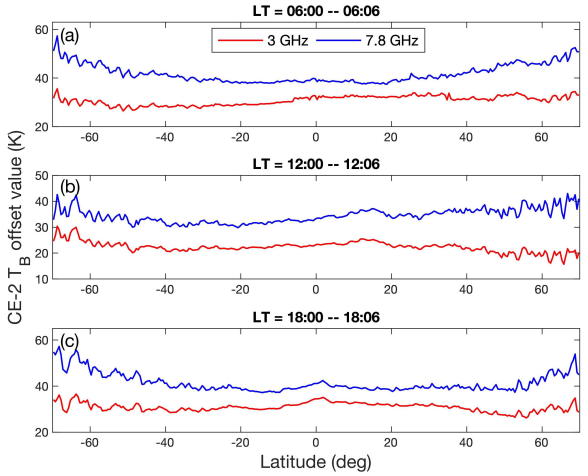

Fig. 6. T_B offset values vary as a function of latitude at LTs of (a) 06:00–06:06, (b) 12:00–12:06, and (c) 18:00–18:06. The offset is averaged from each 0.5° latitude band with the same LT range.

radiometry remote sensing techniques [29], [30]. CE-1's MRM data suggest that the average regolith thicknesses of the maria and highlands are ∼4.5 and ∼7.6 m, respectively [30]. They are greater than the sensed depths of microwaves at 3.0 and 7.8 GHz [31]. Although the above results are not identical, they suggest that global regolith thickness varies from several to more than 10 m. We derive the subsurface temperatures to a depth of 5 m, which is sufficient to represent the total microwave emission through all depths for these two channels.

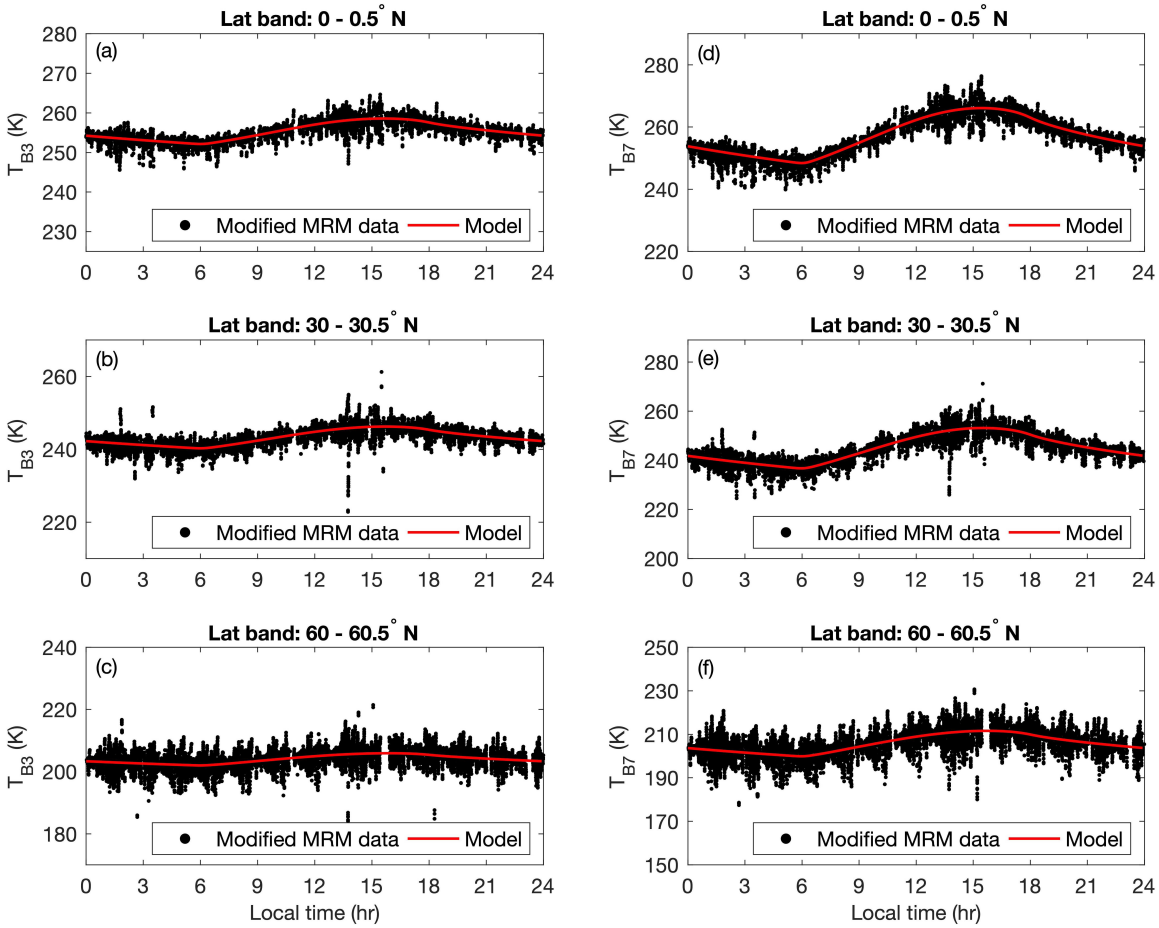

Fig. 7. Comparison between diurnal variations of modified CE-2 MRM data and T_B simulations at (Left column) 3.0 GHz and (Right column) 7.8 GHz. (a) and (d), (b)–(e), and (c) and (f) Latitude bands of 0–0.5° N, 30–30.5° N, and 60–60.5° N, respectively.

The thermal behavior of the subsurface is mainly controlled by the effective solar irradiance of the surface (latitudinal effect), surface topographic relief, and thermophysical properties of regolith. Diurnal variations of subsurface temperatures are different at each cell, especially for different latitudes. For example, the minimum and maximum temperature profiles at 0° E, 0° N and 0° E, 70° N bins differ due to the thermal constraints of $T_{\rm bol}$ and H parameter controlled regolith thermal property (see Fig. 2). It can be seen that the subsurface thermal features in terms of temperature profiles and amplitudes at different places can be characterized by our improved thermal model.

In order to compare subsurface temperatures globally, we calculated instant subsurface temperatures at a given LT. Fig. 3 shows the global distribution of instant subsurface temperatures at the depths of 0.02 m, $T(0, 0.02)$, and 0.1 m, $T(0, 0.1)$. At the first glance, the temperature of the two layers decreases gradually with latitude due to the decreasing solar irradiance. At this LT, temperature increases with depth, but at a rate that differs from place to place. Topography also plays an important role in subsurface temperature at all latitudes and the temperature of the maria is higher than that of the highlands, which can be attributed to the low albedo of those materials. The details of geologic units revealed by the subsurface temperature map, such as the two layers of midnight temperature, suggest the accuracy and effectiveness of our improved thermal model.

B. T_B Simulation and Evaluation

As mentioned above, the improved thermal model makes it possible for us to model microwave brightness temperature accurately at any LT on the Moon. To compare with CE-2 MRM data, we first present both observed data points and modeled T_B values at different latitude bands through all the longitude (180° W–180° E). The bandwidth is set 0.5° to correspond to the $T_{\rm bol}$ spatial resolution. Fig. 4 shows obviously that the absolute amplitude of diurnal variations of CE-2 T_{B3} and T_{B7} (black dots) is much smaller than that of simulations (red solid line). Similar T_B discrepancies have also been reported in [10] and [11]. Note that the simulation within each latitude band was derived by averaging all the bins at the same LT. Adjusting different offset values, the T_B discrepancies of both two channels between observations and adjusted models (red dashed line) vary with LT significantly, especially near 06:00 and 18:00 when the cold horn reorienting toward the Sun [10]. It can be seen that offset values also vary among different latitude bands, which suggests that the calibration uncertainties of CE-2 MRM data are dominated by heat contamination on a global scale [9].

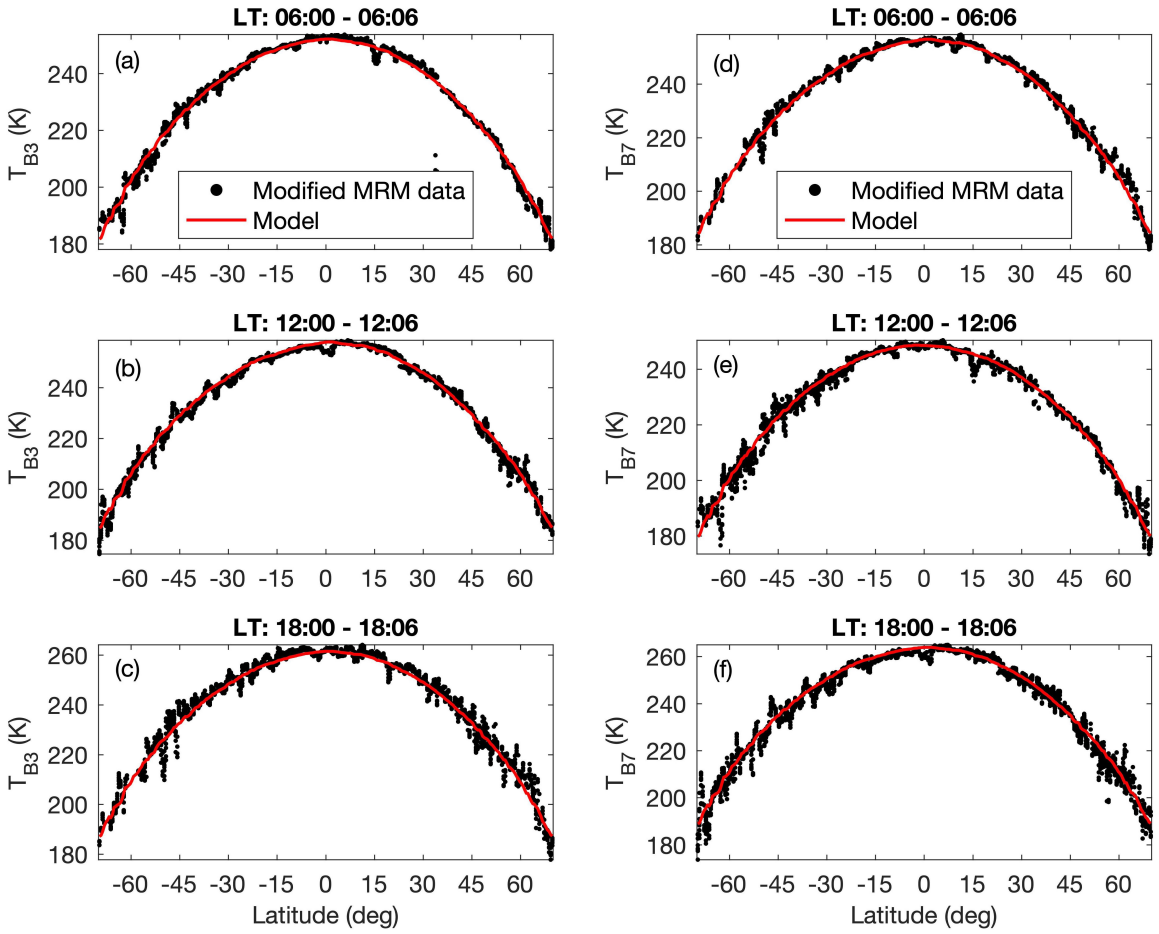

Fig. 8. Comparison between modified CE-2 MRM data and T_B simulations at (Left column) 3.0 GHz and (Right column) 7.8 GHz at different LTs. (a) and (d), (b)–(e), and (c) and (f) LT ranges of 06:00–06:06, 12:00–12:06, and 18:00–18:06, respectively.

As noted above, the adjusted offset at different LTs and latitudes presents a good evaluation for the time- and latitude-dependent global calibration uncertainties. In addition, we derived offset values with LT interval 10 min and latitude interval 0.5°. The 10 min used here is to make sure that there is enough global coverage of CE-2 data points during this period. Fig. 5 shows the offset values of T_{B3} and T_{B7} varying with LTs at different latitudes. Apparently, both the two channels' offset values present larger amplitude near 06:00 and 18:00, which indicates larger T_B calibration uncertainties near terminators. The relatively small offset values near noon and midnight indicate smaller calibration uncertainties, which indicates less heat contaminations [9]. The T_{B7} offset is ∼12 K greater in average than the T_{B3} offset at different latitudes, which suggests larger calibration uncertainties at the 7.8-GHz channel on a global scale. Notably, both T_{B3} and T_{B7} offset values vary with LT in a similar trend due to their identical observation conditions. In addition, both northern (solid lines) and southern (dashed-dotted lines) hemispheres at the same latitude band show a similar trend with increasing of LT, but they still present an absolute mean discrepancy <1.2 K at different latitude bands.

To characterize the latitude-dependent T_B offset, Fig. 6 shows that the offset tends to be asymmetric (higher values at southern latitudes) with increasing latitude, which indicates that the heat contamination is dominated by the regional thermal features [13]. In general, both T_{B3} and T_{B7} offsets present complexly latitude-dependent variation at different LTs, especially at high latitudes (>40° N/S). In addition, the offset difference between the two channels increases from ∼10 K near the equator to ∼20 K at high latitudes. It suggests a complex and different calibration uncertainty of the two channels during the CE-2 mission.

C. Global T_B Modification

As described above, the time- and latitude-dependent offset value presents a better way to evaluate the CE-2 calibration uncertainties quantitatively, that is, each CE-2 MRM data point can be modified by a specific offset based on its observation LT and footprint position. Using the same data as in Fig. 4 and the offset values of Fig. 5, Fig. 7 shows the T_B comparison between diurnal variations of modified CE-2 observations and modeled values within different latitude bands. Here, the modeled values (red line) are the same with that of Fig. 4 (red solid line). Apparently, the modified CE-2 T_B values consist well with our simulations at different latitude bands. It indicates that the time-related calibration uncertainties have been modified effectively, especially near the LT 06:00 and 18:00. Similarly, considering the latitude-dependent offset as shown in Fig. 6,

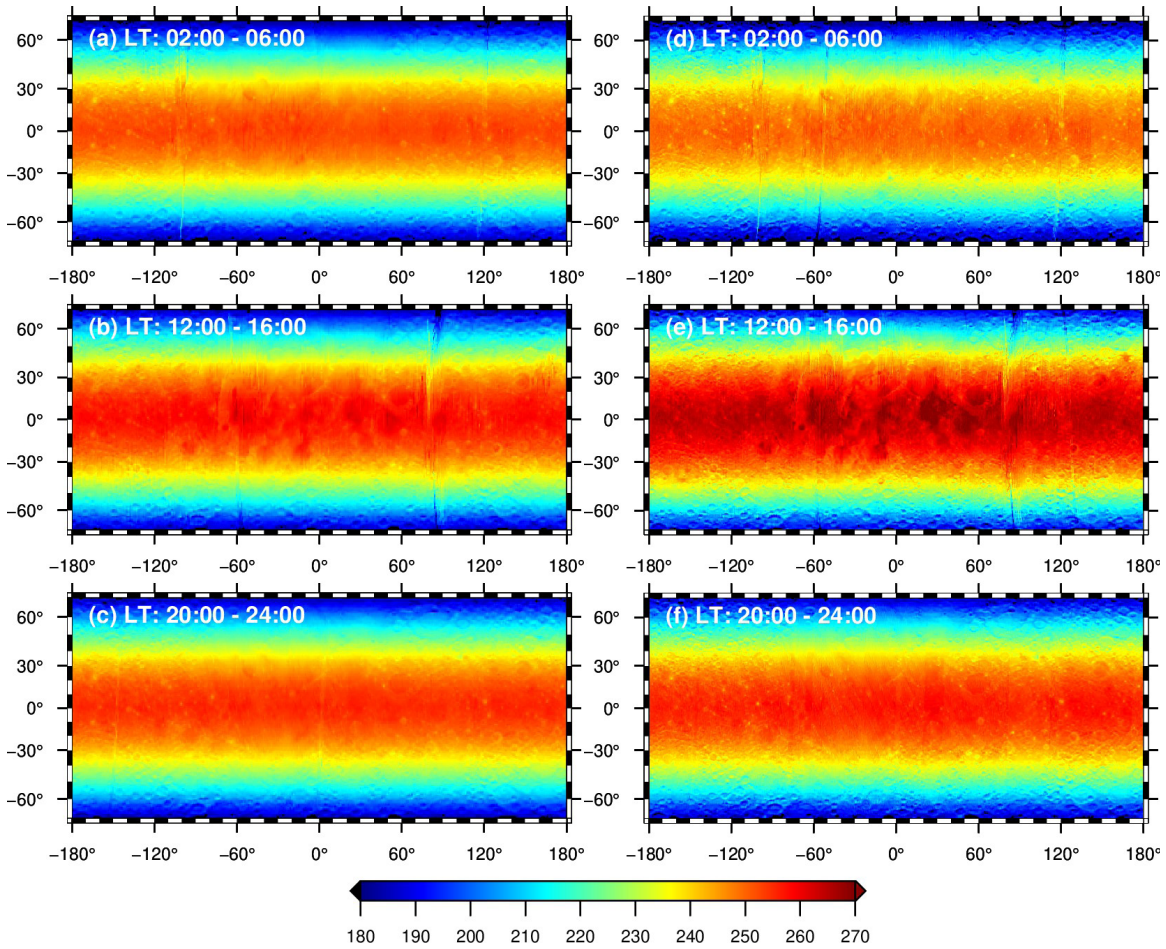

Fig. 9. Global mapped modified T_{B3} (left column) and T_{B7} (right column) at different LT ranges. (a) and (d), (b)–(e), and (c) and (f) LT ranges of 02:00–06:00, 12:00-16:00 and 20:00–24:00, respectively.

for example, Fig. 8 shows that the modified CE-2 MRM data have a good agreement with simulations, especially at high latitudes.

In order to characterize and interpret global thermal environments, we modify the CE-2 T_B data with the time- and latitude-dependent offset values. Fig. 9 shows the global maps of modified T_{B3} (left column) and T_{B7} (right column) within LT range of 02:00–06:00, 12:00–16:00, and 20:00–24:00. It is worth noting that the modified T_Bs are mapped globally with LT interval 2 h due to less coverage of MRM's footprints at any given LT. This will not influence T_B comparisons between different LT ranges in a lunar cycle. It can be seen that the latitude effect dominates the thermal behaviors of the lunar surface at both channels in a lunar day. The modified data can present more accurate thermal features in terms of T_B amplitudes on the Moon. Specifically, many low-T_B spots can be identified in nighttime T_B maps in Fig. 9(a), (c), (d), (f)], especially at shorter wavelength 7.8-GHz maps. In addition, these low-T_B spots have also been identified from CE-2 19.35- and 37-GHz T_B maps [7], [32] that correspond to young rocky craters. The elevated rock concentration causes large loss factors, which suppresses microwave emission significantly than that of nonrocky areas. As a result, global thermal anomalies corresponding to elevated RA can be characterized accurately from modified T_B maps. The detailed investigation of this complex thermal environment will help us to better understand near-surface thermal property and history of rocks broken down and regolith evolution.

For daytime T_B maps [see Fig. 9(b) and (e)], lunar mare presents a distinct thermal behavior than highlands, especially for the high Ti content areas, for example, Oceanus Procellarum (18.4° N, 57.4° W) and Mare Tranquillitatis (8.5° N, 31.4° E). The modified T_B data can provide better thermal constraints to investigate the geologic evolution of these basaltic areas.

V. Discussion

A. Validation and Error Estimation of T_B Simulation

Since there are no a "ground-truth" observations at the same microwave frequency to compare with our modeled T_B, we are unable to recalibrate the CE-2 MRM data and/or validate our simulations directly. It has been reported that the high-frequency channels (19.35 and 37 GHz) have a relatively small calibration uncertainty, which is attributed to the heat contamination [9] but not cold horn reorientation effect [10]. Here, we model T_B at 19.35 (T_{B19}) and 37 GHz (T_{B37}) and then compare it with CE-2 MRM's observations. Fig. 10 shows the T_B comparison between CE-2 MRM data and simulations at

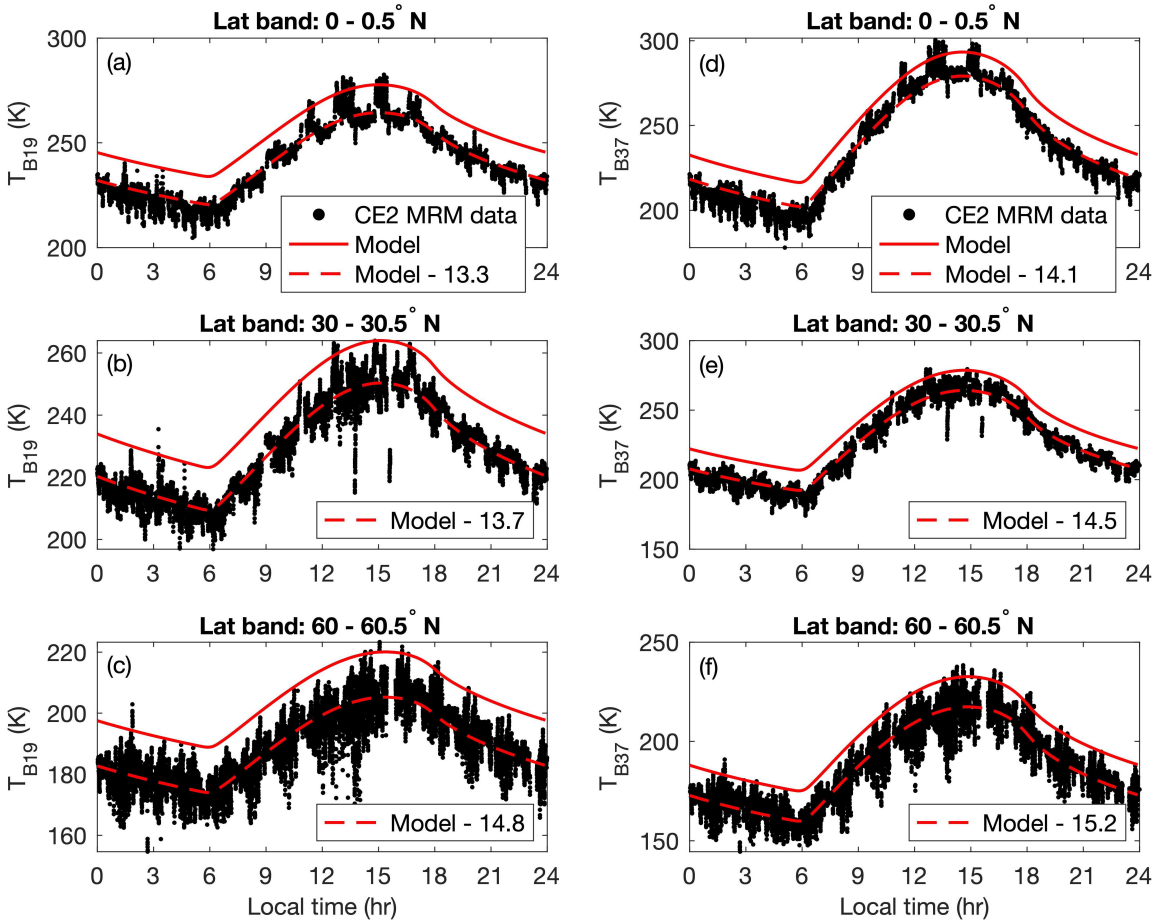

Fig. 10. Comparison of diurnal variation of T_B between CE-2 MRM data and simulations at different latitude bands. (a) and (d), (b)–(e), and (c) and (f) Latitude bands of 0–0.5° N, 30–30.5° N, and 60–60.5° N, respectively.

different latitude bands. It also presents an obvious discrepancy for T_{B19} and T_{B37} at all latitudes in a lunar day. Similarly, we also employ the offset to adjust models. It can be seen that the adjusted models (red dashed lines) present a good consistent with MRM's data at all LTs, especially near the LTs 06:00 and 18:00. Note that the T_{B19} (13.3–14.8 K) and T_{B37} (14.1–15.2 K) offsets agree well with 8.9 ± 8.5 and 11.4 ± 9.6 K (the latitude band of Apollo 15 landing site) and 8.0 ± 8.9 and 10.4 ± 8.9 K (the latitude band of Apollo 17 landing site) of Hu *et al.* [9]. The good agreement between MRM data and adjusted models validates our T_B simulations.

As noted above, the RA effect is neglected in our thermal model and T_B simulations. Thus, the rocky area could cause an additional T_B bias for CE-2 MRM data modification. The exposed and/or perched rocks distribute randomly on the Moon but tend to concentrate at young craters [16]. Here, we derive the averaged rock concentration within each 0.5° latitude band from Diviner RA. Note that the Diviner RA defines the area percentage of rocks within each pixel [16], [33]. Fig. 11 shows in general that the RA decreases from ∼0.46% to ∼0.3% with the increasing of latitude at both hemispheres. Although there is no RA value within 60–70° N/S latitude bands, it can be estimated that the RA within these highland areas is no more than 0.5%. Therefore, it can be inferred that no more than 0.5% of lunar surface with elevated RA might cause additional errors for T_B simulation and CE-2 MRM data modification. Statistically, the <0.5% surface area will not have a great impact on T_B comparison on a global scale. However, for regional scale and/or rocky areas, a more detailed rock model should be considered in the future for T_B simulation and CE-2 MRM data evaluation.

B. Seasonal Effects on T_B Simulations

Because the small tilt of the Moon's spin axis (∼1.54°) relative to the ecliptic plane, the latitude of subsolar point varies with an amplitude of about 1.54°, which causes the seasonal effect. Comparing to the Earth's (23.44°) and Mars' (25.19°) axial tilts, the seasonality has minimal influence on surface temperatures at low-to-mid latitudes but relatively large influence in permanently shadowed regions (PSRs) of the Moon [34], that is, the seasonal effects on modeled T_B at sunlit areas of the Moon can be neglected, while the seasonal variation of surface temperatures at PSRs caused by light scattering and thermal radiation of crater walls [2] should be considered in the future work.

Fig. 12 shows the variation of the subsolar latitude during the CE-2's life span (light red area) and part of LRO's Diviner observations (light blue area). The CE-2's MRM observed

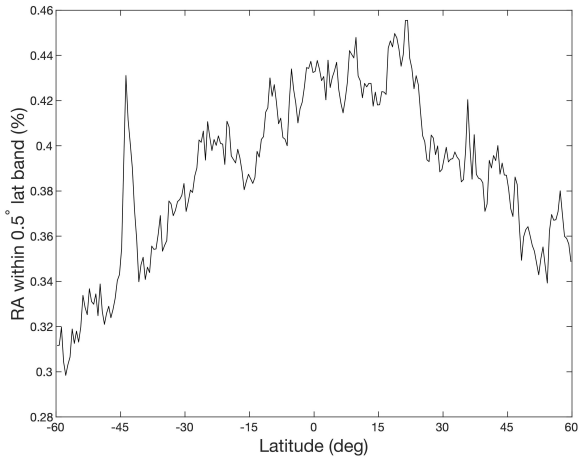

Fig. 11. RA varies with latitude. The RA is derived from the Diviner data by Bandfield *et al.* [16], [33], which is available at the PDS Geoscience Node (https://pds-geosciences.wustl.edu/).

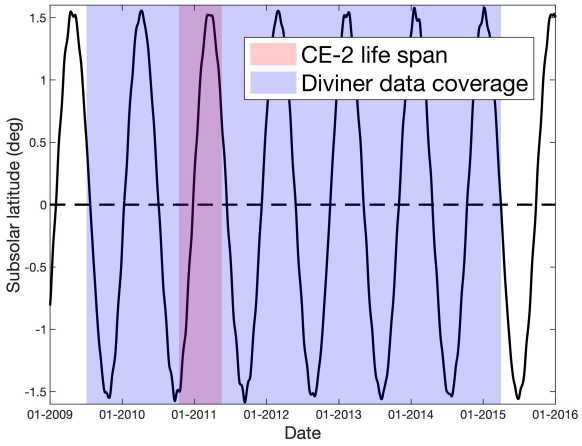

Fig. 12. Variation of subsolar latitude during the CE-2's life span and part of LRO Diviner's observations. The dashed line indicates the equator. The light red area and light blue area indicate the CE-2's life span and part of LRO Diviner's observations, respectively. Note that the Diviner data coverage only refers to the dataset used in this study.

the Moon from northern winter to northern summer though it has a short life span. However, it is worth noting that the near-surface microwave emission in terms of T_B can be measured at a specific LT, 06:00/18:00, for example, in any season. The Diviner dataset used in this study covers the Moon over 5.5 years, which includes multiple seasonal cycles. The annual Diviner observations were combined and redistributed by LTs at each 0.5° × 0.5° bin [15], that is, the seasonal information in terms of surface temperature is involved and "averaged" by diurnal $T_{\rm bol}$ data during the Diviner's multiple measurement periods. Therefore, the modeled T_B constrained by $T_{\rm bol}$ data also includes seasonal information that covers the CE-2's life span. For example, we calculate the diurnal and annual averaged T_{B3} theoretically at the Moon's equator corresponding to the Diviner's ∼5.5 years observations and find that the absolute maximal/minimal T_{B3} during northern summer/winter solstice is ∼1.9 K less than that of seasonal averaged. In the future work, more $T_{\rm bol}$ data obtained in

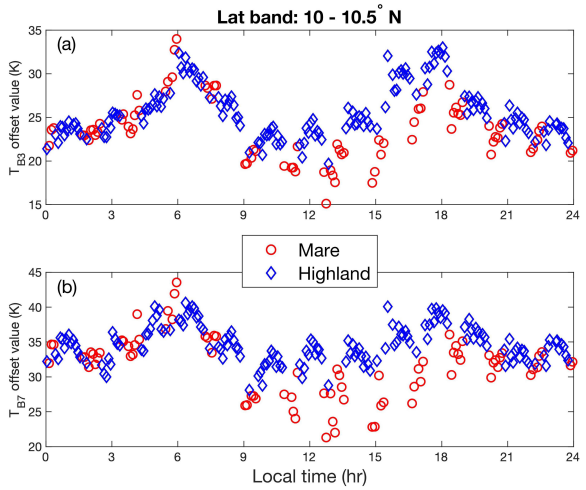

Fig. 13. Variation of T_B offsets as a function of LT within latitude band 10°–10.5° N at (a) 3.0 and (b) 7.8 GHz. The averaged Ti content at mare and highland is ∼4.5% and ∼1.1%, respectively.

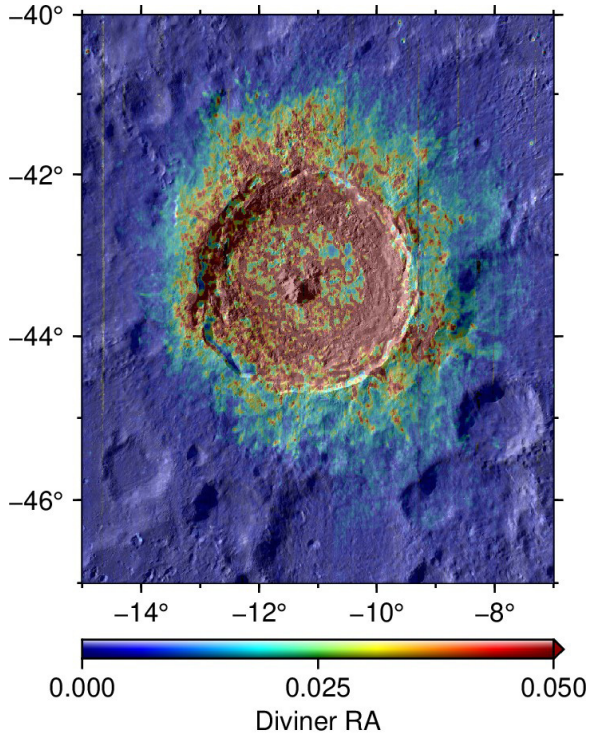

Fig. 14. Diviner RA at Tycho crater. The background is LRO WAC image. Note that the Diviner RA data are retrieved by Bandfield *et al.* [16], [33], which is available at the PDS Geosciences Node.

different seasons can be used to constrain T_B simulations for MRM data evaluation and modification.

C. Effect of Titanium Content on T_B Modification

Both CE-1 and CE-2 MRM observations indicate that the titanium content plays an important role in microwave emission [6], [7]. The effect of Ti content on loss tangent was discussed in detail in the work of [11]. Also, the loss tangent models at maria and highlands were also employed (7) and (8) to model T_B in this work. In order to compare the influence

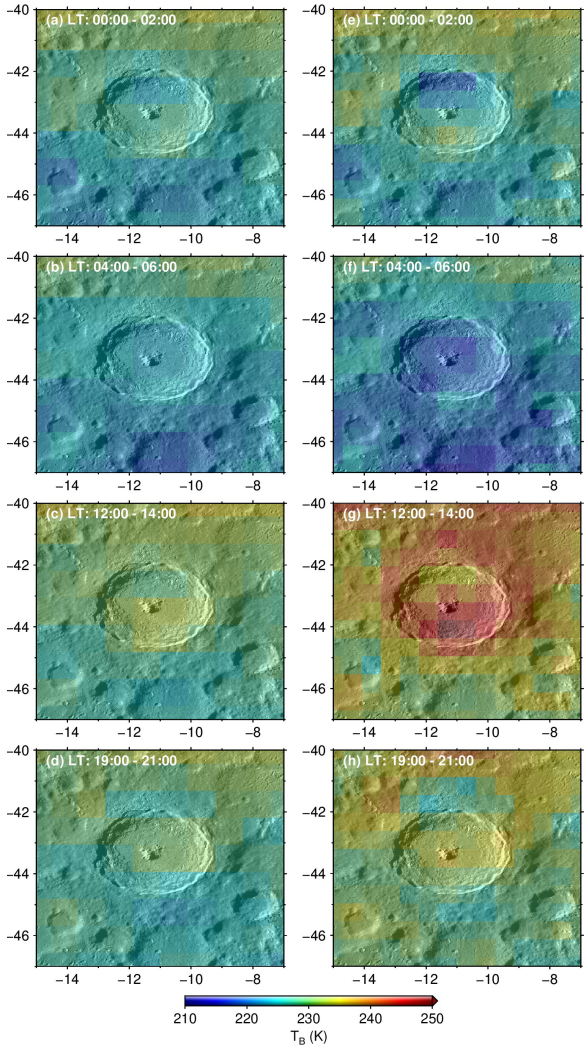

Fig. 15. Distribution of modified T_{B3} (left column) and T_{B7} (right column) at different LTs of Tycho crater. (a) and (e), (b)–(f), (c) and (g), and (d) and (h) LT ranges of 00:00–02:00, 04:00–06:00, 12:00–14:00, and 19:00–21:00, respectively. The background is LRO WAC image.

of Ti content in T_B modification, i.e., T_B offset, we select a latitude band, 10°–10.5° N, which covers both mare and highland areas. The offset values corresponding to each of the CE-2 T_{B3} and T_{B7} data points at different LTs within this band are derived. Fig. 13 shows the comparison of T_B offset values between mare and highland areas at different LTs. These two areas have a good agreement all times However, it presents a large discrepancy from 09:00 to 18:00 between the two channels. Also, the averaged T_{B3} and T_{B7} offsets at highland (blue diamonds) are ∼4.9 and ∼6.9 K higher than that at mare (red circles), respectively. We suppose that the calibration uncertainties of CE-2 MRM data are not related to lunar surface geologic units and composition in the nighttime but are more dependent on the Ti content in the daytime. Note that since we derive the time-dependent offset from a latitude band, the topographic effect within this area can be neglected.

D. Low-T_B Spots—A Case Study of Tycho Crater

Comparing to thermal infrared observations, microwave emissions measured by MRM at different frequencies can reveal more geophysical information about lunar regolith. One of the most interesting investigations is the thermal anomaly, i.e., low-T_B spots. Although many low-T_B spots have been identified by CE-2 MRM data [7], [32], the calibration uncertainties influence the accuracy of data interpretation for these thermal anomalies. In our study, the modified T_B can help us to better understand the near-surface complex thermal emission caused by buried rocks and small fragments in addition to exposed rocks that have been revealed by Diviner RA. Comparing to high-frequency channels (i.e., 19.35 and 37 GHz), the modified low frequency (longer wavelength) can reveal more details of greater depths, which is related to the subsurface thermal regime and thermophysical properties. This section presents a preliminary application, i.e., thermal feature analysis, from our modified T_B data at Tycho crater.

Both Diviner RA and LRO narrow-angle camera images show that young craters concentrate more rocks because of less exposure time and crater degradation [16], [35]. Fig. 14 shows the Diviner RA at Tycho crater and ejecta blankets. The high concentration of rocks at this young impact crater (85^{+15}_{-18} Ma [36]) indicates less destruction of rocks but more complex geomorphology.

Fig. 15 shows the modified T_{B3} and T_{B7} at Tycho crater within different LT ranges. Specifically, it is a close-up of low-T_B spots as shown in Fig. 9 (nighttime maps). The rocky areas present obviously lower T_B during nighttime but higher values in daytime, especially for the 7.8-GHz channel [see Fig. 9(e) and (f)]. Comparing to infrared observations, the modified microwave data corresponding to rocky craters provides us more information about the subsurface thermal behavior and rock concentration, which is related to crater degradation and regolith evolution of the Moon.

VI. Conclusion

CE-2 MRM observations can reveal the subsurface thermal regime, which is dominated by regolith thermophysical properties, chemical composition, and even RAs. However, it has been reported that there are large calibration uncertainties at MRM's low frequencies (3.0 and 7.8 GHz), which influences the accuracy of interpreting lunar near-surface thermal environments and geologic features. In this study, we first improved the thermal model by using the T_{bol} data to constraint diurnal variations of lunar surface temperatures and the H parameter to constrain the bulk density and thermal conductivity of lunar regolith. As a result, we calculated time- and depth-dependent subsurface temperatures effectively on a global scale. We found that the distribution of subsurface temperatures was not only controlled by latitude but also by topographic slopes.

The derived subsurface temperatures enabled us to model T_B globally. We evaluated the CE-2 MRM data by comparing with modeled T_B values on a global scale at different LT ranges and latitude bands. The results showed that the calibration uncertainties offset values of the two channels vary with LT in a similar trend but dramatically near 06:00 and 18:00. We also found that the 7.8-GHz channel presents a higher calibration uncertainty (∼12 K in average) than the

3.0-GHz channel through a lunar day. Furthermore, the global calibration uncertainties of the two channels are more time relevant and less latitude- and composition-dependent.

Finally, we modified the CE-2 MRM data by time- and latitude-dependent T_B offset values. A large number of low-T_B spots corresponding to elevated RA were identified in the nighttime T_B maps, especially for the 7.8-GHz channel, whereas in daytime T_B maps, distinct microwave emission areas corresponding to basaltic areas were identified. The modified CE-2 MRM data can provide us more accurate information to investigate near-surface thermal features that are related to RA, chemical composition, and geologic evolution of lunar regolith.

ACKNOWLEDGMENT

The authors would like to thank Paul O. Hayne, University of Colorado at Boulder, for providing the H parameter dataset and discussing with them about data usage. They would also like to thank two anonymous reviewers for their comments which greatly improved the manuscript. The Diviner T_{bol} dataset and Diviner rock abundance data were obtained from the NASA Planetary Data System (PDS) Geosciences Node, available at http:// pds-geosciences.wustl.edu/missions/lro/diviner.htm. CE-2 MRM data were provided by the Ground Research and Application System of the Chinese Lunar Exploration Program and are available at http://moon.bao.ac.cn.

REFERENCES

[1] S. J. Keihm, "Interpretation of the lunar microwave brightness temperature spectrum: Feasibility of orbital heat flow mapping," *Icarus*, vol. 60, no. 3, pp. 568–589, Dec. 1984.

[2] D. A. Paige *et al.*, "Diviner lunar radiometer observations of cold traps in the Moon's south polar region," *Science*, vol. 330, no. 6003, pp. 479–482, Oct. 2010.

[3] P. O. Hayne *et al.*, "Global regolith thermophysical properties of the Moon from the Diviner lunar radiometer experiment," *J. Geophys. Res., Planets*, vol. 122, no. 12, pp. 2371–2400, Dec. 2017.

[4] W. P. Jones, J. R. Watkins, and T. A. Calvert, "Temperatures and thermophysical properties of the lunar outermost layer," *Moon*, vol. 13, no. 4, pp. 475–494, Dec. 1975.

[5] B. L. Gary and S. J. Keihm, "Interpretation of ground-based microwave measurements of the Moon using a detailed regolith properties model," in *Proc. 9th Lunar Planet. Sci. Conf.*, 1978, pp. 2885–2900.

[6] Y. C. Zheng, K. T. Tsang, K. L. Chan, Y. L. Zou, F. Zhang, and Z. Y. Ouyang, "First microwave map of the Moon with Chang'E-1 data: The role of local time in global imaging," *Icarus*, vol. 219, no. 1, pp. 194–210, May 2012.

[7] Y.-C. Zheng *et al.*, "Analysis of Chang'E-2 brightness temperature data and production of high spatial resolution microwave maps of the moon," *Icarus*, vol. 319, pp. 627–644, Feb. 2019.

[8] Z. Wang *et al.*, "Calibration and brightness temperature algorithm of CE-1 lunar microwave sounder (CELMS)," *Sci. China Earth Sci.*, vol. 53, no. 9, pp. 1392–1406, Sep. 2010.

[9] G.-P. Hu, K. L. Chan, Y.-C. Zheng, K. T. Tsang, and A.-A. Xu, "Comparison and evaluation of the Chang'E microwave radiometer data based on theoretical computation of brightness temperatures at the apollo 15 and 17 sites," *Icarus*, vol. 294, pp. 72–80, Sep. 2017.

[10] J. Feng, M. A. Siegler, and P. O. Hayne, "New constraints on thermal and dielectric properties of lunar regolith from LRO diviner and CE-2 microwave radiometer," *J. Geophys. Res., Planets*, vol. 125, no. 1, Jan. 2020, Art. no. e2019JE006130, doi: 10.1029/2019JE006130.

[11] M. A. Siegler, J. Feng, P. G. Lucey, R. R. Ghent, P. O. Hayne, and M. N. White, "Lunar titanium and frequency-dependent microwave loss tangent as constrained by the Chang'E-2 MRM and LRO diviner lunar radiometers," *J. Geophys. Res., Planets*, vol. 125, no. 9, pp. 31–475, Aug. 2020.

[12] G.-P. Hu, Y.-C. Zheng, A.-A. Xu, and Z.-S. Tang, "Qualitative verification of CE-2's microwave measurement: Relative calibration based on brightness temperature model and data fusion," *IEEE Trans. Geosci. Remote Sens.*, vol. 54, no. 3, pp. 1598–1609, Mar. 2016.

[13] G. Hu *et al.*, "Brightness temperature calculation of lunar crater: Interpretation of topographic effect on microwave data from Chang'E," *IEEE Trans. Geosci. Remote Sens.*, vol. 52, no. 8, pp. 4499–4510, Aug. 2014.

[14] D. A. Paige *et al.*, "The lunar reconnaissance orbiter Diviner lunar radiometer experiment," *Space Sci. Rev.*, vol. 150, nos. 1–4, pp. 125–160, 2010.

[15] J.-P. Williams, D. A. Paige, B. T. Greenhagen, and E. Sefton-Nash, "The global surface temperatures of the Moon as measured by the Diviner lunar radiometer experiment," *Icarus*, vol. 283, pp. 300–325, Feb. 2017.

[16] J. L. Bandfield, R. R. Ghent, A. R. Vasavada, D. A. Paige, S. J. Lawrence, and M. S. Robinson, "Lunar surface rock abundance and regolith fines temperatures derived from LRO Diviner radiometer data," *J. Geophys. Res.*, vol. 116, no. E12, pp. 1–18, Dec. 2011, doi: 10.1029/2011JE003866.

[17] G. Wei, X. Li, H. Gan, D. T. Blewett, C. D. Neish, and B. T. Greenhagen, "A new method for simulation of lunar microwave brightness temperatures and evaluation of Chang'E-2 MRM data using thermal constraints from Diviner," *J. Geophys. Res., Planets*, vol. 116, no. 1, p. E00H02-18, 2019.

[18] A. R. Vasavada *et al.*, "Lunar equatorial surface temperatures and regolith properties from the Diviner lunar radiometer experiment," *J. Geophys. Res., Planets*, vol. 117, no. E12, pp. 1–12, 2012, doi: 10.1029/2011JE003987.

[19] H. Sato *et al.*, "Lunar mare TiO_2 abundances estimated from UV/Vis reflectance," *Icarus*, vol. 296, pp. 216–238, Nov. 2017.

[20] P. G. Lucey, D. T. Blewett, and B. L. Jolliff, "Lunar iron and titanium abundance algorithms based on final processing of clementine ultraviolet-visible images," *J. Geophys. Res., Planets*, vol. 105, no. E8, pp. 20297–20305, Aug. 2000.

[21] J. J. Gillis, B. L. Jolliff, and R. C. Elphic, "A revised algorithm for calculating TiO_2 from clementine UVVIS data: A synthesis of rock, soil, and remotely sensed TiO_2 concentrations," *J. Geophys. Res., Planets*, vol. 108, no. E2, pp. 1–18, 2003, doi: 10.1029/2001JE001515.

[22] D. L. Mitchell and I. de Pater, "Microwave imaging of Mercury's thermal emission at wavelengths from 0.3 to 20.5 cm," *Icarus*, vol. 110, no. 1, pp. 2–32, Jul. 1994.

[23] P. H. Warren and K. L. Rasmussen, "Megaregolith insulation, internal temperatures, and bulk uranium content of the moon," *J. Geophys. Res., Planets*, vol. 92, no. B5, pp. 3453–3465, 1987.

[24] W. D. Carrier, G. R. Olhoeft, and W. Mendell, "Physical properties of the lunar surface," in *Lunar Sourcebook: A User's Guide to the Moon*. New York, NY, USA: Cambridge Univ. Press, 1991, pp. 475–594.

[25] M. Montopoli, A. Di Carlofelice, P. Tognolatti, and F. S. Marzano, "Remote sensing of the Moon's subsurface with multifrequency microwave radiometers: A numerical study," *Radio Sci.*, vol. 46, no. 1, pp. 1–13, Feb. 2011, doi: 10.1029/2009RS004311.

[26] Z. Cai and T. Lan, "Lunar brightness temperature model based on the microwave radiometer data of Chang'E-2," *IEEE Trans. Geosci. Remote Sens.*, vol. 55, no. 10, pp. 5944–5955, Oct. 2017.

[27] T. Lan and Z. Cai, "Lunar brightness temperature map and TB distribution model," *IEEE Trans. Geosci. Remote Sens.*, vol. 56, no. 12, pp. 7310–7323, Dec. 2018.

[28] W. L. Quaide and V. R. Oberbeck, "Thickness determinations of the lunar surface layer from lunar impact craters," *J. Geophys. Res.*, vol. 73, no. 16, pp. 5247–5270, Aug. 1968.

[29] Y. G. Shkuratov and N. V. Bondarenko, "Regolith layer thickness mapping of the moon by radar and optical data," *Icarus*, vol. 149, no. 2, pp. 329–338, Feb. 2001.

[30] W. Fa and Y. Jin, "Analysis of microwave brightness temperature of lunar surface and inversion of regolith layer thickness: Primary results of Chang-E 1 multi-channel radiometer observation," *Sci. China Inf. Sci.*, vol. 53, no. 1, pp. 168–181, Jan. 2010.

[31] T. Fang and W. Fa, "High frequency thermal emission from the lunar surface and near surface temperature of the moon from Chang'E-2 microwave radiometer," *Icarus*, vol. 232, pp. 34–53, Apr. 2014.

[32] Y. Zhu, Y. Zheng, S. Fang, Y. Zou, and S. Pearson, "Analysis of the brightness temperature features of the lunar surface using 37 GHz channel data from the Chang'E-2 microwave radiometer," *Adv. Space Res.*, vol. 63, no. 1, pp. 750–765, Jan. 2019.

[33] J. L. Bandfield *et al.*, "Distal ejecta from lunar impacts: Extensive regions of rocky deposits," *Icarus*, vol. 283, pp. 282–299, Feb. 2017.

[34] J.-P. Williams *et al.*, "Seasonal polar temperatures on the moon," *J. Geophys. Res., Planets*, vol. 124, no. 10, pp. 2505–2521, Oct. 2019, doi: 10.1029/2019JE006028.
[35] R. R. Ghent *et al.*, "Constraints on the recent rate of lunar ejecta breakdown and implications for crater ages," *Geology*, vol. 42, no. 12, pp. 1059–1062, Dec. 2014.
[36] H. Hiesinger *et al.*, "How old are young lunar craters?" *J. Geophys. Research: Planets*, vol. 117, no. E12, pp. 1–15, Dec. 2012.

Guangfei Wei was born in Anhui, China, in 1986. He received the Ph.D. degree in geochemistry from the University of Chinese Academy of Sciences, Beijing, China, in 2015.

He is an Associate Professor with the Center for Lunar and Planetary Sciences, Institute of Geochemistry, Chinese Academy of Sciences, Guiyang, China. His research interests include using microwave and thermal infrared data to investigate the lunar surface thermal environment and regolith thermal property.

Shane Byrne was born in Drogheda, Ireland, in 1975. He received the M.Phys. degree in astrophysics from the University of Wales, Cardiff, U.K., in 1998, and the Ph.D. degree in planetary sciences from the California Institute of Technology, Pasadena, CA, USA, in 2003.

After post-doctoral studies at the Massachusetts Institute of Technology, Cambridge, MA, USA, and the U.S. Geological Survey, Flagstaff, AZ, USA, he joined the faculty of the Lunar and Planetary Laboratory, The University of Arizona, Tucson, AZ, USA, in 2007, where he is a Professor and an Assistant Department Head. He is the Director of the Space Imagery Center, a NASA Regional Planetary Image Facility, which archives planetary spacecraft and telescopic data not available online and conducts outreach events. He specializes in surface processes on planetary bodies especially those that affect, or are driven by planetary ices. He and his research group have over 100 publications covering the Solar System objects ranging from Mercury to Umbriel. He is a Co-Investigator on the HiRISE and CaSSIS cameras at Mars and a Guest Investigator on the Dawn mission at Ceres and a Principal Investigator of technology development awards for Europa Lander Cameras.

Xiongyao Li received the Ph.D. degree in geochemistry from the Graduate University of the Chinese Academy of Sciences, Beijing, China, in 2006.

He is a Professor with the Center for Lunar and Planetary Sciences, Institute of Geochemistry, Chinese Academy of Sciences, Guiyang, China. His research interests include lunar surface thermal environment, space weathering, and solar wind-induced water on the Moon.

Jianqing Feng received the Ph.D. degree in astrophysics from the University of Chinese Academy of Sciences, Beijing, China, in 2015.

He is a Post-Doctoral Research Scientist with the Planetary Science Institute, Tucson, AZ, USA. His research interests include thermal modeling and numerical simulation of brightness temperature of lunar surface in microwave band. He also works on data processing and interpretation of lunar penetrating radar.

Matthew A. Siegler was born in Wayne, IL, USA, in 1981. He received the B.S. degree in physics and film from Cornell University, Ithaca, NY, USA, in 2003, and the Ph.D. degree in geophysics and space physics from the University of California at Los Angeles, Los Angeles, CA, USA, in 2012, with a focus on lunar polar volatile stability.

From 2012 to 2015, he held a post-doctoral position and was a Staff Scientist at the California Institute of Technology's Jet Propulsion Laboratory in the geophysics group specializing in thermal processes and geothermal heat. Since 2015, he has been a Research Scientist with the Planetary Science Institute, Tucson, AZ, USA, and a Research Faculty Member at Southern Methodist University, Dallas, TX, USA. He is a mission Co-Investigator on the Lunar Reconnaissance Orbiter, InSight, OSIRIS-REx, Mars 2020, and Viper missions. His main research interests include solar system volatiles, regolith properties, geothermal heat flow, thermal instrumentation, and infrared microwave remote sensing.